scientific reports

Check for updates

OPEN

# Optical fiber sensor based on Lossy-mode resonance for tamoxifen detection and sensing applications

Fardin Sadeghfar[1], Roghaieh Parvizi[2,3] & Moladad Nikbakht[1]✉

**In this study, we report a novel, eco-friendly optical fiber biosensor for tamoxifen (TAM) detection, featuring a single functional layer of cerium dioxide ($CeO_2$) nanoparticles integrated with a molecularly imprinted polymer (MIP). The $CeO_2$ nanoparticles were synthesized via a green chemistry route using oak fruit extract, yielding nanomaterials with a high refractive index and excellent charge-transfer properties. These unique optical features of $CeO_2$ significantly enhance the lossy mode resonance (LMR) phenomenon by strengthening the fiber's evanescent field, resulting in improved sensitivity and resonance stability. The MIP, synthesized through a facile, surfactant-free, one-step polymerization of polystyrene spheres, serves as the selective recognition layer, ensuring targeted binding of TAM without interfering with the LMR optical response. The MIP/$CeO_2$ nanocomposite was uniformly coated onto a curved optical fiber surface, and the resulting sensor was thoroughly characterized using FESEM, XRD, AFM, FT-IR, and UV-Vis spectroscopy. These analyses confirmed the successful formation of a porous, TAM-selective MIP layer and the effective incorporation of $CeO_2$ nanoparticles. The sensor demonstrated rapid adsorption/desorption kinetics and high permeability, enabling swift and sensitive TAM detection. Under optimal conditions, the LMR-based fiber optic sensor achieved a sensitivity of 12.052 nm/μM with a correlation coefficient ($R_2$) of 0.988. The proposed biosensor shows strong potential for sensitive, selective, and sustainable detection of tamoxifen in pharmaceutical and clinical applications.**

**Keywords** Biosensor, Green chemistry, Lossy mode resonance, Optical fiber, Tamoxifen drug

A fiber optic sensor is a type of sensor that uses the optical fiber itself as a means of transmitting the signal from the remote sensor to the electronics that process the signals. A sensor based on an optical fiber converter works based on the evanescent wave phenomenon. A growing wave refers to a wave that exponentially decays from the core of an optical fiber into the surrounding medium. This occurs when the light traveling within the fiber undergoes total internal reflection at an angle greater than the critical angle. These changes can be detected and related to the concentration or presence of the analyte of interest[1]. Improving the evanescent wave in the uncoated region of the optical fiber is necessary to achieve high sensitivities and low detection limits. This can be done by modifying the optical properties of the fiber or by adding nanostructured layers that can enhance absorption or attenuation of light by the analyte[2]. Advances in biosensors based on LMR have been made for various applications such as medical diagnostics, food safety, and environmental monitoring[3]. Among them, a planar waveguide platform based on microfluidic LMR, which was investigated with the detection of anti-immunoglobulin G (anti-IgG) using a $TiO_2$ thin film as the sensing layer[3]. The change of the thickness of the layers and the radiation angle in the trend of the LMR peaks in the geometry of two layers (ITO + Ag) and three layers (ITO + Ag + ITO) have been evaluated[4].

TAM is used to treat and prevent breast cancer from worsening. Different types of sensors have been designed to detect this drug in pharmaceutical formulations or biological samples. The advancements of these sensors include a membrane potentiometric sensor with a linear response to the ion pair of TAM and phosphomolybdate and the concentration range of this drug is $9.1 \times 10^{-7}$ and $1 \times 10^{-1}$ M, the sensitivity and detection limit of this sensor is $42.9 \pm 0.3$ mV/decade and $7.3 \pm 0.4 \times 10^{-7}$ M respectively[5]. Biosensors using MIP have been evaluated for sensitive and rapid detection[6–8]. An electrochemical MIP sensor with a

[1]Department of Physics, University of Zanjan, Zanjan, Iran. [2]Department of Physics, College of Sciences, Yasouj University, Yasouj, Iran. [3]James Watt School of Engineering, University of Glasgow, Glasgow G12 8QQ, UK. ✉email: mnik@znu.ac.ir

phenylene diamine-resorcinol mixture based on electropolymerization in the presence of template molecules was deposited on the electrode surface. Reduction of ferricyanide peak to TAM drug concentration (1-100 nM), showed linear dependence[9]. The cellular toxicity of TAM has been investigated using impedance biosensors to understand the response of HeLa cells to different doses of TAM without studying its side effects[10]. MIP are used as recognition elements in the design of sensors, because they have higher thermal stability than biological receptors, reusable and higher selectivity than biological receptors[11,12]. These polymers can mimic the function and structure of antibodies and biological receptors and identify target molecules with high sensitivity and selectivity. Some other applications of sensors based on MIP are: detection of biomarkers, drugs, hormones, environmental pollution and toxins in biological samples[13–15], quality control and food tracking and detection of bacteria, viruses, fungi and allergens citeLin2018. The $CeO_2$ nanoparticles have been synthesized by green chemistry method for biomedical applications (diagnostic and therapeutic)[16], using Pometia pinnata[17], Morinda tinctoria plant extract[18], Gloriosa superba L leaf extract, honey and Olea Europaea leaf extract[19]. In addition to mitigating environmental pollution, the green chemistry synthesis method significantly enhances the physical and chemical properties[20].

An electrochemical biosensor based on $CeO_2$ has been reported as a sensitive material with high selectivity in a wide range of concentrations for glucose[21]. The use of $CeO_2$ as a biocompatible and non-toxic material, and the active surface and increased reaction speed, that make it suitable for electrochemical biosensing application[22]. The $CeO_2$ has a high refractive index and a high dielectric constant[23,24]. This can improve the performance and stability of electronic devices that use $CeO_2$ as a dielectric layer. Biosynthesis of composite materials such as nanocrystalline cerium (IV) oxide or nanoceria shows new horizons in the field of medicine as a unique material. The combination of these nanoparticles with MIP by facilitating their bioavailability highlights the applications of these nanoparticles, including tissue regeneration, drug delivery and gene therapy, theranostics and medical imaging[25].

In this research, $CeO_2$ nanoparticles were used by green synthesis method based on molecular imprinted polymer for biosensor applications on optical fiber to detect TAM drug. Refractive index and dielectric constant of the real and imaginary parts were investigated using the transmission spectrum. Sensitivity and selectivity, detection limit, quantification limit and imprinting factor were evaluated in this biosensor.

## Materials and methods

### Materials and devices

The materials and reagents used in this study were carefully selected to ensure the highest quality and purity. Styrene ($C_6H_5CHCH_2$), a key monomer for polymer synthesis, was supplied by Seebio (China). Polyethylene glycol (PEG, $C_{2n}H_{4n+2}O_{n+1}$) was procured from Urokom (China), serving as a stabilizer or surfactant due to its amphiphilic nature. Cerium nitrate hexahydrate ($Ce(NO_3)_3 \cdot 6H_2O$) was obtained from Sigma-Aldrich (USA), commonly used as a precursor for synthesizing cerium-based nanoparticles.

Oak fruits were collected from the Zagros mountain range in Yasuj County. The fruits, characterized by their multiple husks, were manually separated from their outer layers. Following separation, the fruits were exposed to sunlight for one month to ensure complete drying. Once dried, the fruits were ground into a fine powder and stored in powdered form for subsequent extraction procedures.

Solvents such as acetone ($CH_3COCH_3$), ethanol ($C_2H_6O$), and methanol ($CH_4O$) were sourced from Merck KGaA, Germany. These solvents are essential for dissolving reagents and facilitating chemical reactions. The initiator 2,2-azobis(isobutyramide) dihydrochloride (AIBA) was also obtained from Merck KGaA, playing a crucial role in free radical polymerization processes. Sodium hydroxide (NaOH) from the same supplier can be used to adjust pH levels or facilitate hydrolysis reactions.

Tamoxifen citrate, referred to here simply as TAM, was acquired from Wockhardt Limited, England. This drug is primarily known for its use in breast cancer treatment but can be explored in drug delivery systems due to its therapeutic properties. Distilled water was utilized throughout the experiments to ensure purity and minimize contamination risks.

Polymer optical fibers were utilized in this study for their potential in developing advanced sensors. Their flexibility and biocompatibility make them suitable for integration into sensing systems, particularly those requiring precise light transmission and detection. The use of polymer optical fibers enables the creation of innovative sensor solutions that can effectively monitor various parameters by leveraging optical interactions, which is crucial for applications such as biosensing and chemical detection.

To analyze the surface morphology and elemental composition of the samples, a field emission scanning electron microscope (FESEM), model SIGMA VP-500 from ZEISS (Germany), along with an energy dispersive spectroscopy (EDS) and mapping detector from Oxford Instruments (England), were utilized. The crystalline structure and Miller indices were determined using an X-ray diffractometer (XRD), model X'Pert Pro from Panalytical. The presence of functional groups was assessed via a Fourier-transform infrared spectrometer (FTIR), model Spectrum Two from PerkinElmer. Porosity measurements were conducted using a BELSORP mini II porosity meter from Japan, and drug release profiles were monitored with a UV-Vis spectrophotometer (Perkin-Lambda 25, USA). Surface roughness was evaluated using an atomic force microscope (AFM), model WITec from Germany.

### Optical fiber selection and surface preparation

In this study, a polymer optical fiber with a diameter of 750 $\mu$m and a refractive index of 1.49 was selected as the sensing platform. The polymer optical fiber was chosen due to its advantages including low cost, ease of portability, mechanical flexibility (non-fragility), and wide availability, making it suitable for practical biosensing applications. To enable the generation of LMR, the sensing region of the fiber was carefully prepared by etching and polishing. Specifically, the fiber surface was polished using 2000-grit sandpaper to remove surface

irregularities such as bumps and ridges, ensuring a smooth and uniform interface for subsequent coating. This surface treatment is critical to enhance the adhesion and uniformity of the nanocomposite layer and to optimize the evanescent field interaction necessary for LMR.

## Synthesis of cerium dioxide ($CeO_2$) Nanoparticles

To prepare the extract, 10 grams of oak fruit powder were mixed with 100 mL of deionized (DI) water. The mixture was subjected to agitation using a shaker for one hour at $60^\circ C$. After agitation, the mixture was filtered to separate the liquid extract from solid residues. The obtained extract was stored in a refrigerator at $4^\circ C$ for further experimental use.

The oak fruit extract plays a dual role in the green synthesis of $CeO_2$ nanoparticles, acting as both a reducing agent and a stabilizer during the co-precipitation process. The polyphenols and flavonoids present in the extract facilitate the reduction of cerium ions and control the nucleation and growth of the nanoparticles, resulting in smaller and more uniform particle sizes compared to conventional chemical synthesis. Additionally, the organic constituents of the extract influence the crystallization pathway, promoting the formation of high-purity cubic fluorite-phase $CeO_2$, as confirmed by XRD analysis.

For the synthesis of $CeO_2$ nanoparticles (NPs), a 0.1 M solution of cerium nitrate ($Ce(NO_3)_2 \cdot 6H_2O$) was prepared by dissolving it in double-distilled water. A 5 mL aliquot of the oak fruit extract was added dropwise to the 0.1 M cerium nitrate solution while continuously stirring at room temperature. As the reaction progressed and the dosage of oak fruit extract increased, the color of the precipitate changed from purple to light yellow, indicating the formation of $CeO_2$ NPs.

The resulting precipitate was centrifuged and thoroughly washed several times with double-distilled water and acetone, then dried at $70\,^\circ C$ for 1 hour. The dried powder was subsequently calcined and annealed at $400\,^\circ C$ for 2 hours using a furnace to obtain the $CeO_2$ NPs.

## Synthesis of molecularly imprinted polymers (MIPs) and non-imprinted polymers (NIPs)

The synthesis of MIPs involved the polymerization of styrene monomer and TAM in a water/methanol solution (10:1 v/v). The reactor system comprised a 300 mL four-necked flask equipped with a magnetic stirrer, a heating mantle, a cooling condenser, a thermometer for temperature control, and a nitrogen gas inlet to create an inert atmosphere. Initially, 200 mL of double-distilled water was placed in the reactor and maintained at a constant temperature of $70\,^\circ C$ while stirring at 700 rpm under nitrogen to eliminate oxygen and prevent premature polymerization.

To remove inhibitors from styrene, the monomer was washed with a 1 M sodium hydroxide (NaOH) solution. Subsequently, 0.4 wt.% of styrene monomer and 0.5 g of TAM were introduced into the reactor, maintaining the same conditions for 15 min to ensure thorough mixing. The polymerization process was initiated by adding 0.04 wt.% of the initiator 2,2-azobis(isobutyramidine) dihydrochloride (AIBA) to the reaction mixture at $70\,^\circ C$, where it was allowed to react for 24 h. After the reaction period, the resulting solution was cooled to room temperature and stored in a refrigerator at approximately $15\,^\circ C$ for further analysis. For the synthesis of the non-imprinted polymer (NIP), the same method was employed as for the MIP, but without the addition of TAM as the template molecule. This approach ensures that the MIP is selectively tailored to recognize TAM, while the non-imprinted polymer serves as a control polymer for comparative studies. The choice of solvents and conditions is critical in MIP synthesis since they influence the morphology and binding properties of the final polymer. The use of water/methanol as a solvent not only facilitates the solubility of both TAM and styrene but also aids in achieving optimal interaction between the functional monomers and the template molecule during polymerization.

## Synthesis of MIPs/$CeO_2$ and coating optical fiber

The synthesis of MIP/CeO2 nanocomposites was conducted for structural and optical studies. The MIP/$CeO_2$ nanocomposite consists of MIPs integrated with $CeO_2$ nanoparticles, combining selective recognition with enhanced optical properties. The preparation of MIP/CeO2 nanostructures involved a two-step process. Initially, the synthesized $CeO_2$ nanoparticles and MIP were placed separately in an ultrasonic bath for one hour to ensure thorough mixing and dispersion of the materials. Following this, the two solutions were combined, and the mixture was stirred on a magnetic stirrer for an additional hour to achieve a uniform blend. The immobilization of the MIP/$CeO_2$ nanocomposite onto the optical fiber surface was performed as follows: First, $CeO_2$ nanoparticles (20 mg) and the synthesized MIP (20 mg) were each dispersed in 10 mL deionized water and sonicated for 1 h to ensure uniform dispersion. The two suspensions were then combined and stirred magnetically for 1 h. To facilitate stable coating, 20 mL of 0.01 M polyethylene glycol (PEG) solution was added dropwise as a stabilizer and adhesion promoter. The optical fiber was cleaned with acetone and deionized water, then immersed in the composite mixture and subjected to ultrasonication at $70\,^\circ C$ for 45 min to promote uniform deposition. After coating, the fiber was washed thoroughly with deionized water and acetone to remove any unbound material and dried at $80\,^\circ C$ for 4 h. This protocol is adapted from established nanocomposite immobilization methods on optical fibers[26–28]. The optical fiber itself was also thoroughly washed multiple times with deionized water and acetone to eliminate any loosely attached particles that could affect its optical properties. The entire synthesis process is illustrated in Fig. 1, which depicts both the preparation of MIP/$CeO_2$ nanostructures and the subsequent coating of the optical fiber.

## Methodology for evaluating sensitivity and selectivity detection

Tamoxifen solutions were prepared at concentrations ranging from 0.1 $\mu$M to 20 $\mu$M in phosphate-buffered saline (PBS). For each concentration, the transmission spectrum of the MIP/$CeO_2$-coated optical fiber was

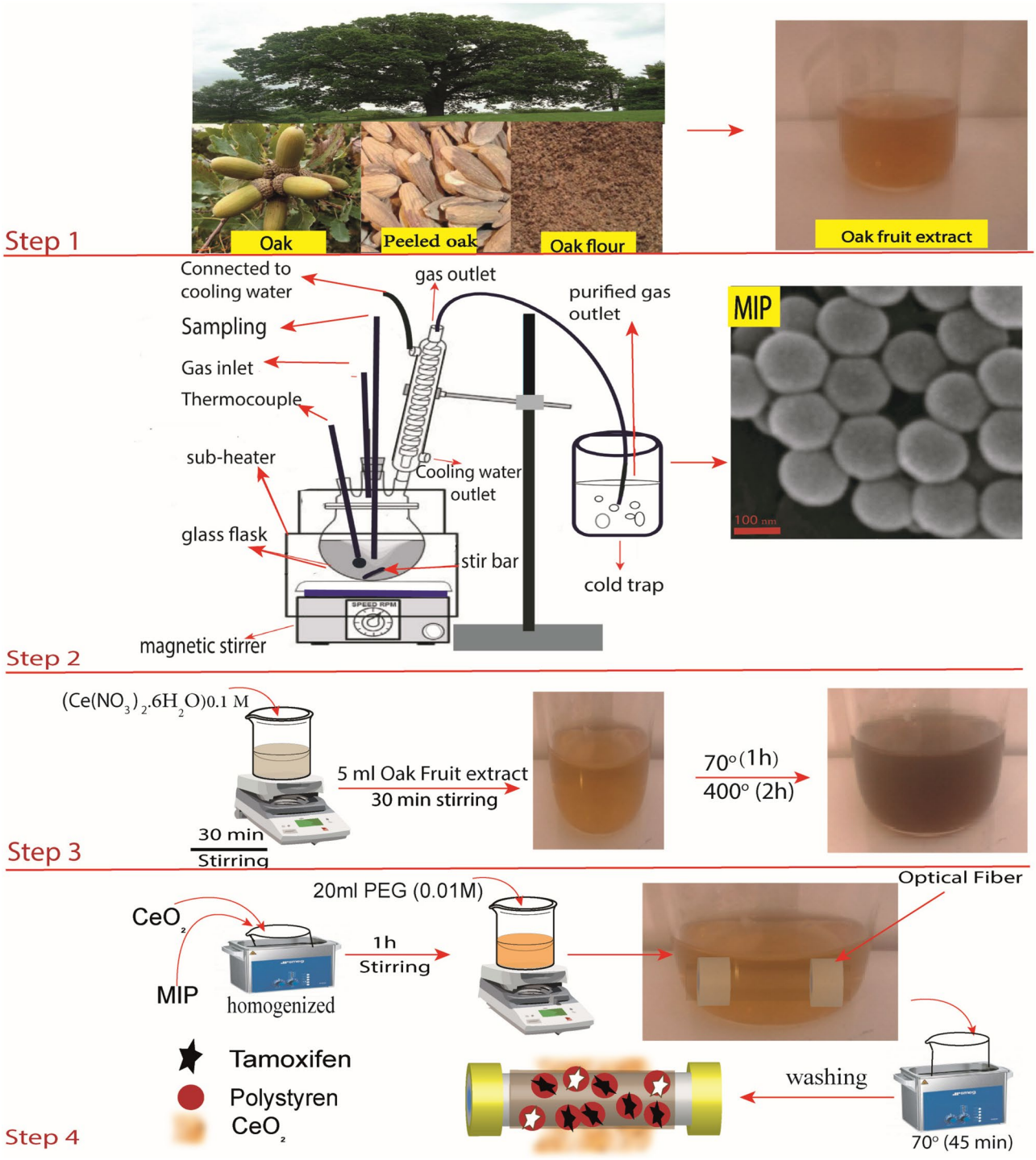


**Fig. 1**. Synthesis and deposition process of MIP/$CeO_2$ nanocomposites on optical fibers, including the steps of mixing, coating, ultrasonication, and subsequent washing to ensure optimal adherence and structural integrity.

recorded using UV–Vis spectroscopy. The interaction of TAM with the MIP layer alters the local refractive index, resulting in a red-shift of the LMR peak.

To evaluate selectivity, the sensor's response to TAM was tested in the presence of potential interfering species, including dopamine (DA), epinephrine (EP), and glucose (Glu). Interferents were tested at the same concentration as TAM (20 $\mu$M) to ensure comparable conditions. Selectivity was further assessed by comparing the response of the MIP/$CeO_2$ sensor to a NIP/$CeO_2$ control sensor. The imprinting factor (IF) is a key parameter used to evaluate the efficiency and selectivity of the molecular imprinting process in MIP-based sensors. It quantifies the enhancement in analyte recognition provided by the imprinted polymer compared to a non-

imprinted control[29]. The imprinting factor is calculated from IF = $\frac{R_{MIP}}{R_{NIP}}$ where $R_{MIP}$ and $R_{NIP}$ represent the response ratios of the MIP/$CeO_2$ and NIP/$CeO_2$ sensors, respectively.

### Measurement of dielectric constant

The limits of detection (LOD) and quantification (LOQ) are critical parameters for evaluating the sensitivity of biosensors, particularly in the context of TAM detection. In this study, the LOD and LOQ were determined using the equations $\mathrm{LOD} = \frac{3.3 \cdot S_b}{\mathrm{slope}}$ and $\mathrm{LOQ} = \frac{10 \cdot S_b}{\mathrm{slope}}$, respectively, where $S_b$ represents the standard deviation of the response and "slope" refers to the sensitivity of the TAM detection curve[28,30].

### Measurement of dielectric constant

The dielectric constant is a critical parameter in material characterization, particularly in optical and electromagnetic applications. It is closely related to the refractive index ($\mathrm{N} = \mathrm{n} + \mathrm{ik}$), where *n* represents the real part and *k* the imaginary part of the refractive index[31]. These components are essential for understanding light-matter interactions and are crucial for the LMR production process. The refractive index (*n*) can be calculated from the transition spectrum using the following equation:

$$n = \sqrt{N + \sqrt{N^2 - S^2}}, \tag{1}$$

where *N* is defined as:

$$N = 2S\left(\frac{T_M - T_m}{T_M T_m}\right) + \frac{S^2 + 1}{2}. \tag{2}$$

Here, $T_M$ and $T_m$ denote the maximum and minimum values of the transmission spectrum, respectively, while *S* represents the refractive index of the optical fiber.

The imaginary part of the refractive index (*k*) is determined from the absorption coefficient $\alpha(\lambda)$ as follows:

$$k(\lambda) = \frac{\alpha(\lambda)}{4\pi\lambda}, \tag{3}$$

where $\alpha(\lambda)$ is expressed as:

$$\alpha(\lambda) = \frac{-\ln(x)}{d}. \tag{4}$$

Here, *d* is the thickness of the coating layer on the optical fiber and the parameter *x* is calculated using:

$$x = \frac{E_m - \sqrt{E_m^2 - (n^2 - 1)^3 - (n^2 - S^4)}}{(n-1)^3(n - S^2)}, \tag{5}$$

and $E_m$ is given by:

$$E_m = \frac{8n^2 S}{T_M} + (n^2 - 1)(n^2 - S^2). \tag{6}$$

To determine the real ($\varepsilon_r$) and imaginary ($\varepsilon_i$) components of the dielectric constant, the following relationships are used:

$$\varepsilon_r = n^2 - k^2, \tag{7}$$

$$\varepsilon_i = 2nk. \tag{8}$$

These equations provide a comprehensive framework for calculating both parts of the dielectric constant, which are essential for evaluating a material's optical and electromagnetic properties.

## Results and discussion

### FTIR spectrum analysis

Fourier-transform infrared (FTIR) spectroscopy was employed to analyze the chemical composition and functional groups present in cerium dioxide and non-imprinted polymer nanoparticles[32,33]. As illustrated in Fig. 2a, the FTIR spectrum for NIP exhibits characteristic peaks corresponding to various molecular vibrations. Notably, a peak at 2960 $cm^{-1}$ is attributed to the stretching vibrations of CH bonds, indicative of alkane groups. Additional bands observed at 1601 $cm^{-1}$ correspond to C=C stretching, while peaks at 1494 $cm^{-1}$ and 1451 $cm^{-1}$ are associated with -CH3 and -$CH_2$ bending vibrations, respectively. Furthermore, the stretching vibrations of C-O-(H) are identified around 1066 $cm^{-1}$ and 1024 $cm^{-1}$. The FTIR spectrum of the synthesized MIP/$CeO_2$ nanoparticles was recorded over a range of 450–4000 $cm^{-1}$, allowing for the identification of various chemical bonds and functional groups within the composite material. A prominent broad band at 3398 $cm^{-1}$ is observed, corresponding to O-H stretching vibrations from hydroxyl groups, which may indicate the presence of moisture or surface hydroxylation on the nanoparticles. The peaks at 2911 $cm^{-1}$ and 2848 $cm^{-1}$ are attributed

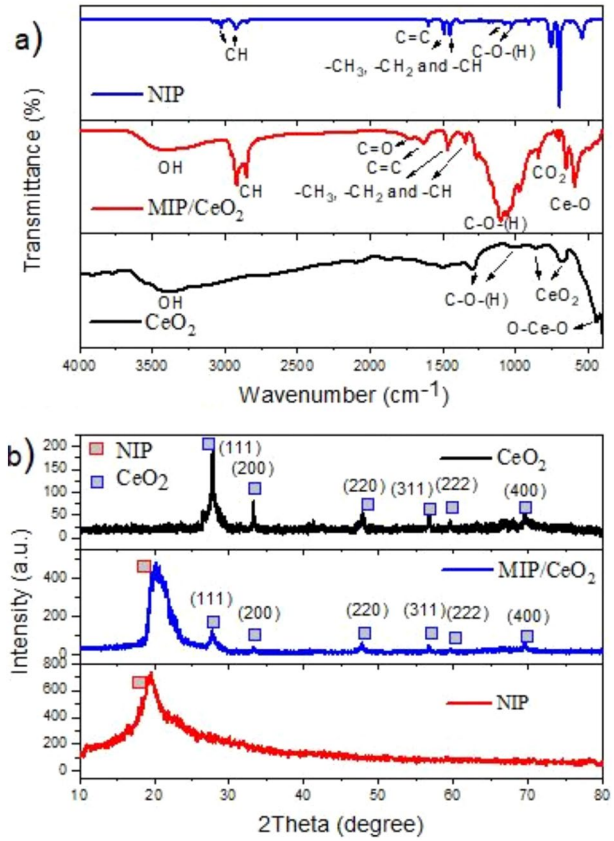


**Fig. 2**. (**a**) FTIR spectrum of NIP and MIP/$CeO_2$ nanocomposites, highlighting characteristic functional groups and bonding interactions. (**b**) XRD patterns of NIP and MIP/$CeO_2$, showing the crystalline phases of the materials, including the broad peak indicative of the amorphous structure of NIP and distinct diffraction peaks corresponding to the face-centered cubic phase of $CeO_2$ nanoparticles.

to C-H stretching vibrations, further confirming the organic components within the nanocomposite. Additional peaks at 1729 $cm^{-1}$ and 1624 $cm^{-1}$ are assigned to C=O and C=C double bond absorptions, respectively. The absorption peaks around 1463 $cm^{-1}$ and 1344 $cm^{-1}$ are linked to bending vibrations of -CH3 and -CH2 groups. Importantly, an intense band at 583 $cm^{-1}$ corresponds to Ce-O stretching vibrations, which are characteristic of cerium oxide materials. Moreover, bands located at approximately 1262 $cm^{-1}$, 1087 $cm^{-1}$, and 1051 $cm^{-1}$ are attributed to C-O-C asymmetric stretching vibrations, while a band at 831 $cm^{-1}$ is associated with $CO_2$. The observed shifts in these bands provide evidence for the hybridization of imprinted polymer particles within the MIP matrix. The FTIR analysis not only confirms the successful synthesis of MIP/$CeO_2$ nanocomposites but also highlights the interactions between the polymer matrix and cerium dioxide nanoparticles. In Figure 2a, the FTIR spectrum of $CeO_2$ shows a band at 1558 $cm^{-1}$ corresponding to the O–H vibration of water molecules. The bands at 657 $cm^{-1}$ and 845 $cm^{-1}$ can be attributed to characteristic $CeO_2$ vibrations. The large absorption band around 420 $cm^{-1}$ is due to the O–Ce–O vibration. Additionally, the broad bands observed near 1320 $cm^{-1}$ and 1048 $cm^{-1}$ are associated with the formation of carbonate species on the $CeO_2$ surface. Such interactions are crucial for optimizing the optical properties and stability of the nanocomposites for potential applications in sensors and photonic devices.

## XRD analysis

X-ray diffraction (XRD) was employed to identify the crystalline phases of the synthesized materials[34]. The XRD patterns were recorded over a $2\theta$ range of $10^\circ$ to $80^\circ$ using an X-Pert Pro MPD diffractometer with Cu-K$\alpha$ radiation ($\lambda = 1.54$ Å). As shown in Figure 2b, the XRD pattern for non-imprinted polymer exhibits a broad reflection peak at $19.491^\circ$, which is indicative of the amorphous structure characteristic of NIP spheres.

Following the deposition of $CeO_2$ nanoparticles, XRD analysis was performed on the MIP/$CeO_2$ composite and $CeO_2$. The diffraction peaks corresponding to the synthesized $CeO_2$ nanoparticles and MIP/$CeO_2$ composite are prominently displayed in Fig. 2b. The observed peaks at specific $2\theta$ values are as follows: $28.681^\circ$ (111), $33.280^\circ$ (200), $47.835^\circ$ (220), $56.783^\circ$ (311), $59.599^\circ$ (222), and $69.583^\circ$ (400). These diffraction peaks align well with the standard reference pattern from the Joint Committee on Powder Diffraction Standards (JCPDS card No: 01-0800), confirming the presence of the typical face-centered cubic phase of $CeO_2$ nanoparticles.

The sharpness and intensity of these peaks suggest a well-defined crystalline structure, indicating that the $CeO_2$ nanoparticles were successfully synthesized and deposited onto the MIP matrix. Such structural

characterization is crucial for understanding the material properties and potential applications in various fields, including catalysis and photonics.

## FESEM-mapping analysis

Field emission scanning electron microscopy (FESEM) was utilized to investigate the morphology and elemental composition of the synthesized nanoparticles, as well as to perform elemental mapping on their surfaces. The results are presented in Fig. 3. Figure 3a displays the morphology of the MIP surface at a scale of 100 nm, revealing that all non-imprinted polymer nanoparticles are spherical in shape, with an average diameter of approximately 120 nm. This uniformity in size is crucial for ensuring consistent performance in applications such as drug delivery and sensor technology.

Figure 3b illustrates the morphology of the MIP/$CeO_2$ composite at a scale of 200 nm. Here, $CeO_2$ nanoparticles, averaging about 30 nm in size, are observed to be well-dispersed on the MIP surface. The effective

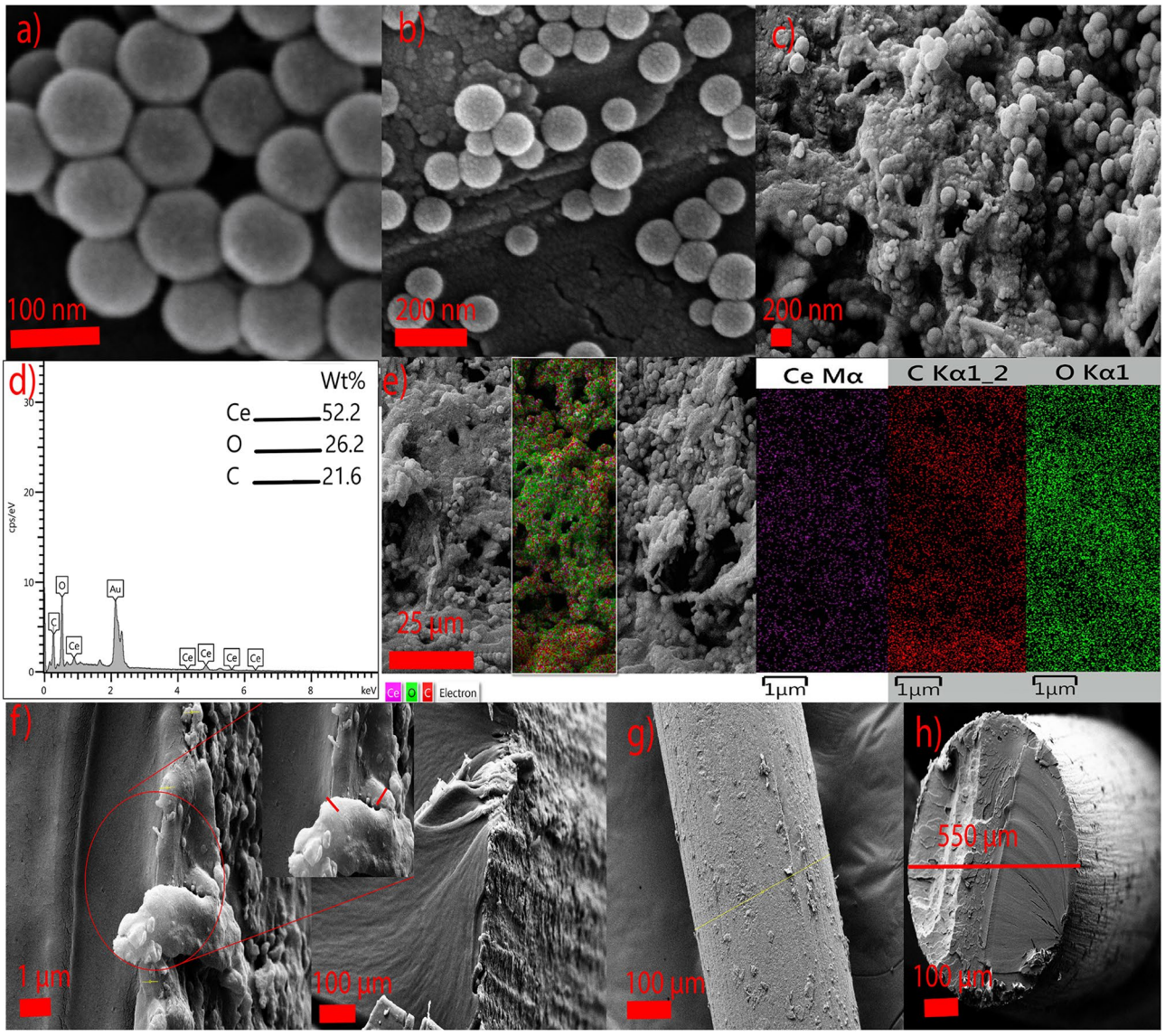


**Fig. 3**. Field emission scanning electron microscopy (FESEM) images showcasing the morphology and elemental analysis of the synthesized nanocomposites: (**a**) molecular imprinted polymer (MIP), (**b**) molecular imprinted polymer MIP/$CeO_2$, and (**c**) molecular imprinted polymer MIP/$CeO_2$-TAM, highlighting the spherical shape and size distribution of nanoparticles. (**d**) Energy-dispersive X-ray spectroscopy (EDX) analysis indicating the elemental composition of MIP/$CeO_2$, with approximate percentages of cerium (Ce), oxygen (O), and carbon (C). (**e**) Elemental mapping of MIP/$CeO_2$ demonstrating the uniform distribution of elements across the nanostructure. (**f**) Cross-sectional view of the MIP/$CeO_2$ layer on the optical fiber, showing a thickness of approximately 590 nm. (**g**) Measurement of the optical fiber diameter in the sensing area, approximately 550$\mu$m, where the MIP/$CeO_2$ nanostructured layer is applied, and (**h**) Cross-section of optical fiber before coating.

attachment of $CeO_2$ nanoparticles enhances the composite's properties, potentially improving its catalytic activity and stability.

In Figure 3c, the MIP/$CeO_2$-TAM surface is shown at a scale of 200 nm. The TAM drug is seen to coat the surface of the MIP/$CeO_2$ nanostructure, indicating successful drug loading. This stable surface adsorption is essential for achieving controlled release profiles in therapeutic applications.

Figure 3d presents the elemental composition of the MIP/$CeO_2$ nanostructure as determined by energy-dispersive X-ray spectroscopy (EDX). The analysis reveals that the composite contains carbon (C), oxygen (O), and cerium (Ce) as its primary elements. The quantitative EDX results are summarized in Table 1, showing both weight and atomic percentages for each element. This elemental distribution confirms the successful integration of $CeO_2$ nanoparticles within the polymer matrix and is critical for understanding the material's functionality and reactivity.

Elemental mapping results are depicted in Fig. 3e, showcasing the spatial distribution of elements within the MIP/$CeO_2$ nanostructure. The distinct color compositions indicate that both oxygen and cerium are uniformly dispersed across the surface of the MIP, which is advantageous for enhancing the material's catalytic properties.

Figure 3f illustrates the thickness of the MIP/$CeO_2$ nanostructure layer on the optical fiber within the sensing area. The cross-sectional view obtained through FESEM at a magnification of 1 $\mu$m and 100 *mu*m shows that this layer is approximately 590 nm thick. This thickness is significant as it influences both sensitivity and response time in sensor applications.

Additionally, Fig. 3g provides measurements of the optical fiber's diameter in the sensing region, which is approximately 550 $\mu$m where the MIP/$CeO_2$ nanostructured layer has been applied. Understanding these dimensions is vital for optimizing sensor design and ensuring compatibility with existing systems.

The cross-sectional image of the 550 $\mu$m etched optical fiber before coating (Fig. 3h) reveals a precisely modified surface that enhances light interaction, thereby improving sensing performance. The etching process removes the cladding, exposing the core to external influences, optimizing LMR sensitivity. This structural refinement ensures efficient optical transmission and facilitates uniform nanocomposite adhesion.

## TEM analysis

Transmission electron microscopy (TEM) was utilized to investigate the size and morphology of $CeO_2$ nanoparticles synthesized using oak fruit extract. The TEM images, presented in Fig. 4, reveal the structural characteristics of the nanoparticles at two distinct scales of 30 nm and 80 nm, corresponding to panels (a) and (b), respectively. In Fig. 4c, the particle count based on size for the synthesized $CeO_2$ nanoparticles is analyzed. According to the graph and experimental results, the particle sizes range and standard deviation between 12.18 ± 1 nm and 95.07 ± 1 nm, with the highest size frequency observed at approximately 19.01 ± 1 nm. The zeta potential measurements for the $CeO_2$ nanoparticle solution are presented in Fig. 4d, which shows a peak zeta potential value of − 13.6 mV. The $CeO_2$ nanoparticles predominantly exhibit a spherical morphology, with an average diameter of approximately 30 nm. This size is critical as it influences the nanoparticles' surface area-to-volume ratio, which is essential for enhancing catalytic activity and reactivity in various applications, including environmental remediation and drug delivery. The uniformity in size distribution observed in the TEM images indicates effective synthesis conditions, minimizing agglomeration and ensuring that the nanoparticles retain their individual properties. Such characteristics are vital for applications where consistent particle size can affect performance, such as in catalysis or as additives in polymer matrices.

## AFM analysis

Atomic force microscopy (AFM) was employed to assess the surface roughness of the optical fiber after etching, which is critical for optimizing the performance of fiber optic sensors. The roughness of the fiber surface significantly influences the intensity of transmitted light, as it affects the attenuation of the evanescent wave in the sensor region. In this study, approximately 27% of the optical fiber was etched using a mechanical device in conjunction with 2000-grit sandpaper to achieve a controlled surface profile.

Figure 5 presents the roughness measurements for the etched area, displayed in both 2D and 3D formats with dimensions of 800 nm × 800 nm. The AFM analysis revealed that the surface roughness in the etched regions varies from 0 to 4.637 nm. This variation is crucial as it directly impacts the output light intensity and sensitivity response of the optical fiber sensor. A smoother surface typically enhances light transmission efficiency, while increased roughness can lead to scattering losses.

The AFM images provide detailed insights into the topographical features of the etched fiber surface, allowing for quantitative assessment of roughness parameters such as root mean square roughness (Rq) and average roughness (Ra). These metrics are essential for evaluating how surface characteristics influence sensor performance. The precise measurement capabilities of AFM enable accurate profiling of surface irregularities at the nanoscale, which is vital for applications requiring high sensitivity and specificity. The Ra was determined to be 0.7673 nm, and the root mean Rq was measured as 1.062 nm. These param eters were evaluated over the

| Element | Weight (%) |
|---|---|
| C | 21.6 |
| O | 26.2 |
| Ce | 52.2 |

**Table 1**. Elemental composition of the MIP/$CeO_2$ layer by EDX (corresponding to Fig. 3d).

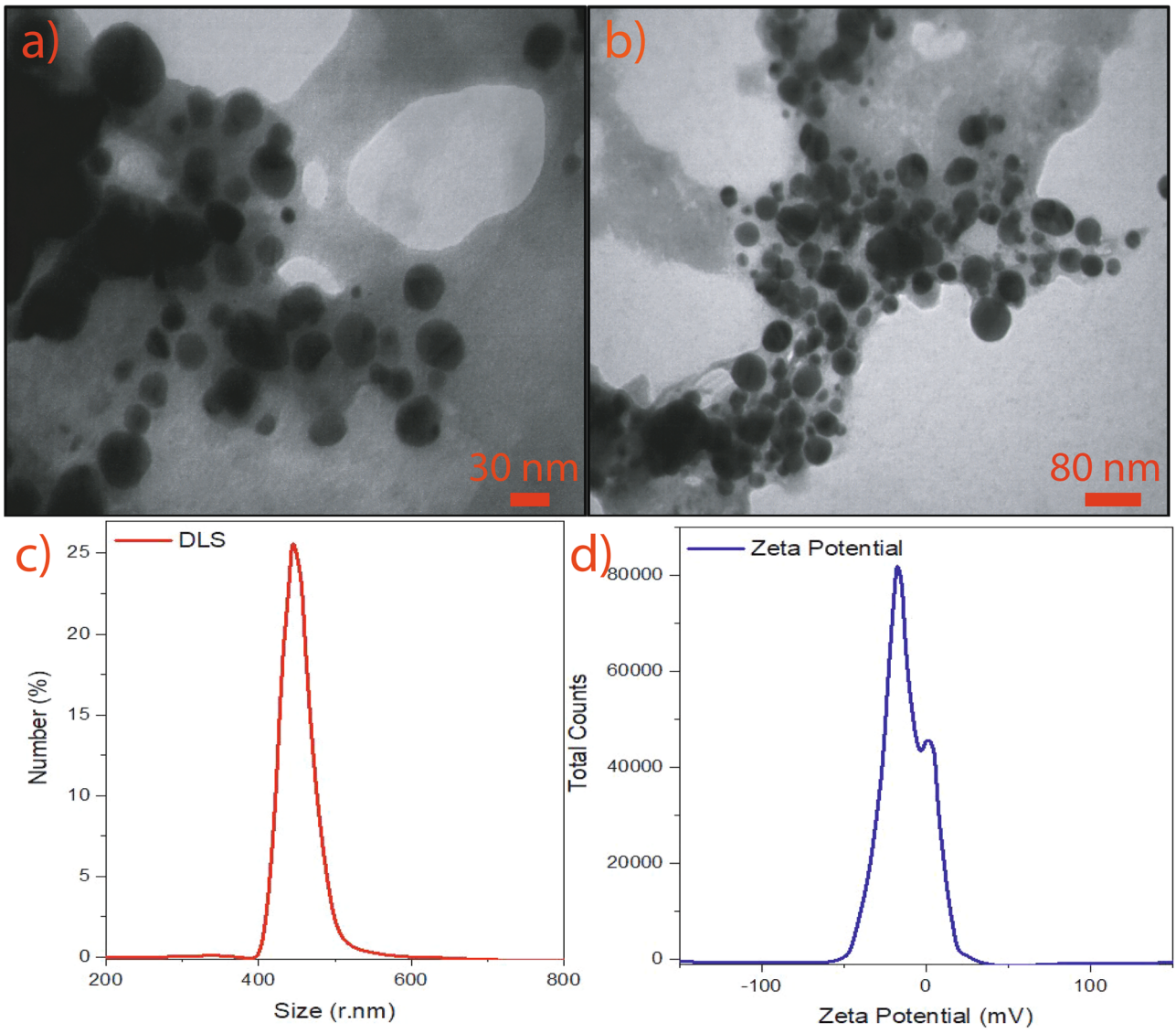


**Fig. 4**. Transmission electron microscopy (TEM) images of $CeO_2$ nanoparticles, illustrating their morphology at two distinct scales: (**a**) 30 nm and (**b**) 80 nm. The nanoparticles predominantly exhibit a spherical shape, with an average diameter of approximately 30 nm, indicating effective synthesis and uniform size distribution. (**c**) Dynamic light scattering (DLS) and (**d**) zeta potential.

etched area of the optical fiber to quantify the surface texture that influences the evanescent wave interaction and overall sensor performance.

In conclusion, AFM analysis not only confirms the effectiveness of the etching process in modifying the optical fiber's surface but also provides critical data on surface roughness that is essential for optimizing sensor performance. Unde

## Sensor characterization

*Lossy-mode response of MIP/$CeO_2$ nanostructure*

Figure 6 illustrates the transmission spectrum of the MIP/$CeO_2$ nanostructure, which has been coated as a thin layer on the surface of an optical fiber with a diameter of 550 $\mu$m and a refractive index of 1.49. Panels (a) and (b) depict the optical transmission spectrum alongside the dielectric constants, including both the real and imaginary components, of the MIP/$CeO_2$ nanostructure acting as the sensing region.

Analysis of the transmitted light spectrum reveals significant changes in both the real part ($n$) and imaginary part ($k$) of the refractive index. The dielectric constant can be expressed as $\varepsilon = \varepsilon_r + i\varepsilon_i$, where $\varepsilon_r$ represents the real part and $\varepsilon_i$ denotes the imaginary part. The positivity of $\varepsilon_r$ and the condition $|\varepsilon_i| < |\varepsilon_r|$ indicate the presence of lossy modes in the system.

Notably, the rate of reduction in refractive index for the MIP/$CeO_2$ nanostructure between 475 nm and 575 nm is greater than that observed from 575 nm to 700 nm. This behavior correlates with an increasing trend in the imaginary part within this wavelength range. Consequently, electromagnetic waves exhibit stronger

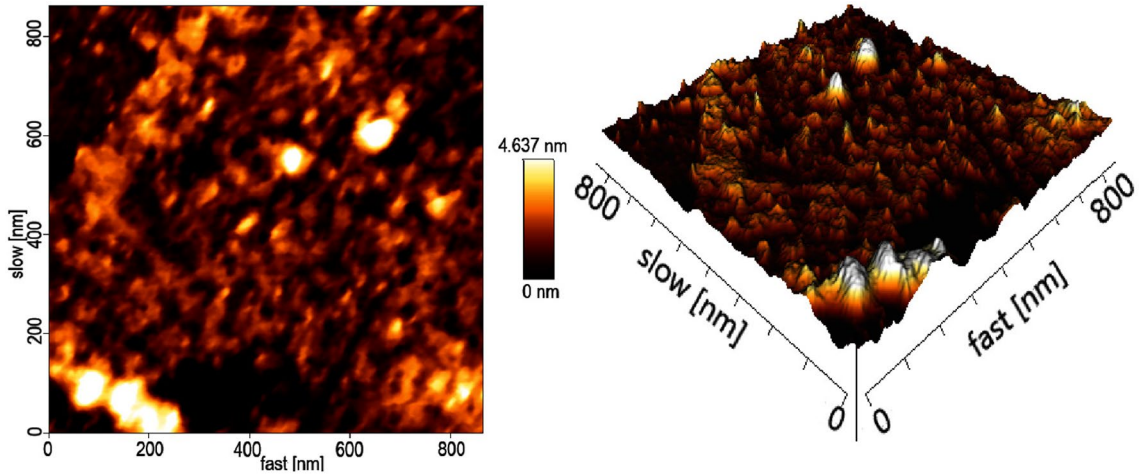


**Fig. 5**. Atomic force microscopy (AFM) analysis of the optical fiber surface after etching, showing the roughness characteristics. The images illustrate the surface topology of the bare optical fiber polished with a mechanical device and 2000-grit sandpaper. The measured roughness in the etched areas ranges from 0 to 4.637 nm, which is critical for optimizing light transmission and sensitivity in fiber optic sensors.

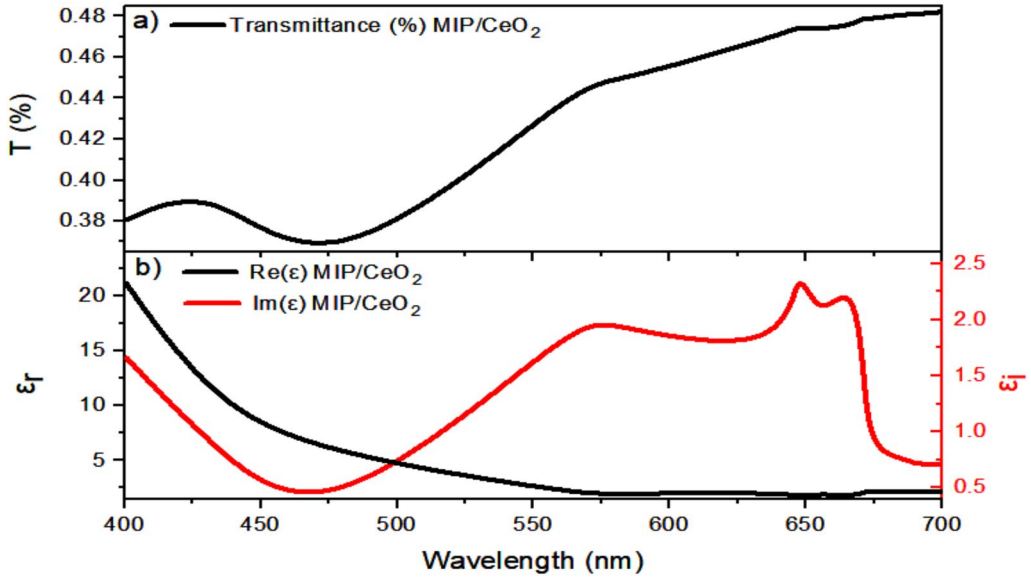


**Fig. 6**. Optical transmission characteristics of the MIP/$CeO_2$ nanostructure coated on an optical fiber. (**a**) Transmission spectra demonstrating the light transmission properties across a range of wavelengths. (**b**) Dielectric constants showing both the real and imaginary parts, indicating how changes in these properties affect the lossy-mode resonance (LMR) response in the sensing region.

interactions with TAM, leading to shifts in the resonance wavelength associated with LMR. Specifically, within the wavelength range of 620 nm to 650 nm, a decreasing trend in the real part of the dielectric function is observed, accompanied by an increase in the imaginary part. This decrease signifies a reduced capacity for energy storage within the material and suggests a lower propagation speed for electromagnetic waves through it.

As a result, confined waves can interact more intensely with their surrounding environment, enhancing LMR resonance. Simultaneously, an increase in $\varepsilon_i$ denotes heightened energy absorption and dissipation within the material. This increased absorption contributes to greater energy loss and enhances damping of resonance modes, resulting in a broader and more pronounced resonance peak observed in the LMR spectrum.

*MIP/$CeO_2$ nanostructure coated optical fiber sensing performance*

The detection of TAM molecules using the LMR optical fiber method based on MPIs represents a highly sensitive and selective approach. MIPs are engineered receptors with specific binding sites designed to capture

TAM molecules with high affinity. By integrating MIPs onto the surface of the optical fiber, a sensor is created that selectively interacts with TAM, resulting in spectral changes in the LMR.

In this sensing mechanism, the optical fiber coated with MIP acts as the sensing element. When TAM molecules in the surrounding environment bind to the MIPs, they induce changes in the local refractive index, leading to a shift in the LMR resonance wavelengths of the optical fiber. These shifts are directly proportional to the concentration of TAM and can be quantitatively measured[35].

Figure 7a and b display the logarithmic transmission spectrum and normalized transmission spectrum in terms of wavelength, respectively. The performance of the optical fiber biosensor, enhanced by the MIP/$CeO_2$ coating, demonstrates a pronounced LMR phenomenon characterized by a shift in the resonant wavelength ($\lambda_{res}$) towards longer wavelengths. The resonant wavelength is defined as the central wavelength corresponding to the slope of the optical transmission spectrum.

The sensitivity of the sensor is quantified as the ratio of the change in resonant wavelength to changes in TAM concentration. The observed shifts in $\lambda_{res}$ are attributed to variations in refractive index differences between guided modes in the optical fiber core and leaky evanescent waves interacting with the surrounding coated nanoparticles. Specifically, an increase in TAM concentration leads to alterations in both refractive indices within the optical fiber and evanescent waves present in the MIP/$CeO_2$ nanostructure.

The response of sensitivity concerning transmission spectra was evaluated over time relative to TAM concentrations. Notably, a shift of 25 nm in $\lambda_{res}$ was observed corresponding to varying concentrations of TAM. Figure 7c illustrates these changes in $\lambda_{res}$ plotted against the logarithm of TAM concentration, allowing for an expression of biosensor sensitivity based on the slope of this relationship[28,36]. The calculated sensitivity (slope) and correlation coefficient ($R^2$) for concentrations ranging from 0.1 to 20 $\mu$M were determined to be 12.052 nm/$\mu$M and 0.988, respectively.

These findings underscore the effectiveness of MIP/$CeO_2$ nanostructured coatings for enhancing optical fiber sensor performance, particularly for low-concentration analyte detection such as TAM. The integration of

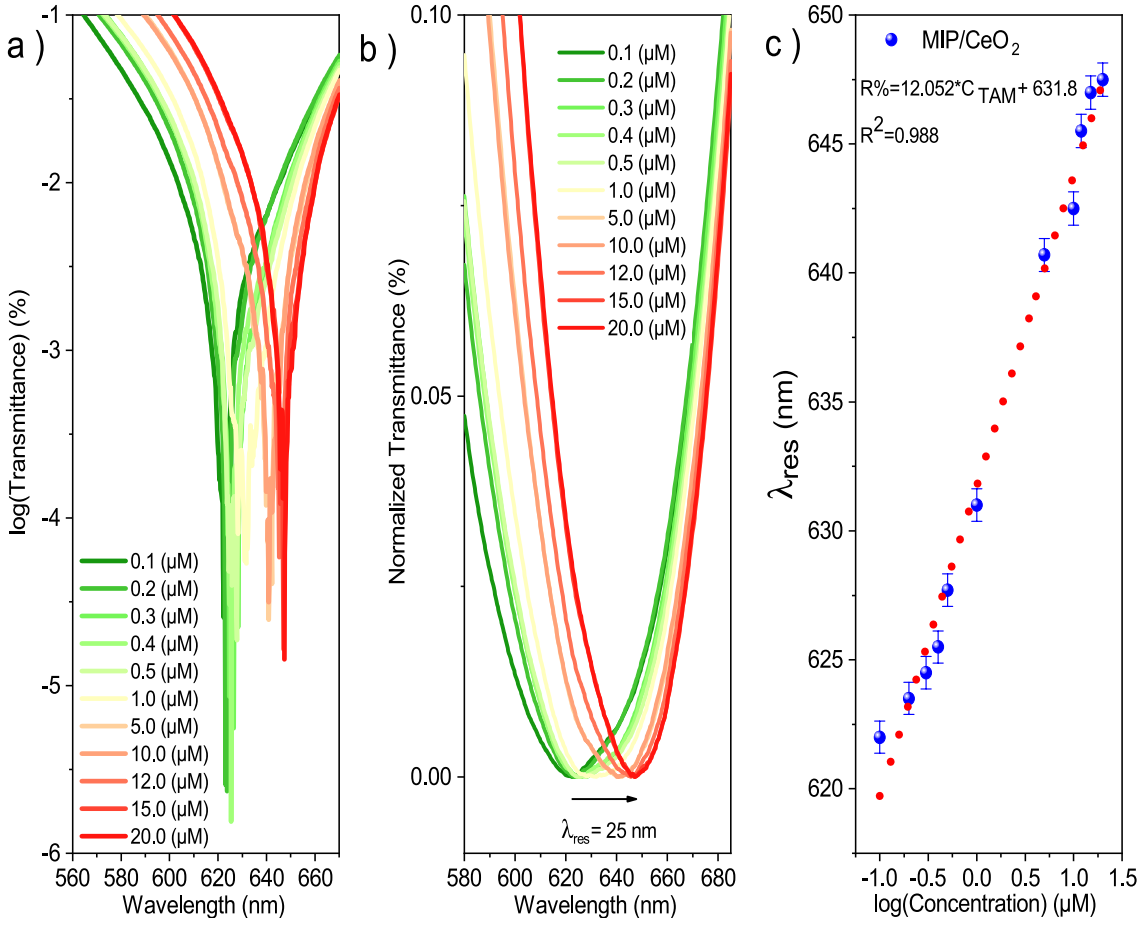


**Fig. 7**. Optical sensing performance of the MIP/$CeO_2$ nanostructure coated optical fiber. (**a**) Logarithmic transmittance spectrum illustrating the relationship between transmittance and wavelength. (**b**) Normalized transmittance spectrum, providing a clearer view of spectral changes. (**c**) Variation of resonance wavelength ($\lambda_{res}$) as a function of the logarithm of TAM drug concentration, demonstrating the sensor's sensitivity and response to varying TAM levels. The observed shifts in $\lambda_{res}$ indicate strong interactions between TAM and the MIP/$CeO_2$ sensing layer, which enhance detection capabilities.

MIPs into optical fiber sensors not only improves selectivity but also significantly enhances sensitivity, making this approach promising for applications in biomedical diagnostics and environmental monitoring.

*Detection selectivity*

The selective permeability of optical fiber sensors is crucial for accurately controlling which substances interact with the sensor, thereby enabling precise measurements and sensitive detection. Figure 8a illustrates the selectivity of the MIP/$CeO_2$ nanostructure under experimental conditions, specifically at a TAM concentration of 20 $\mu$M, alongside potential interfering substances such as Ep, DA, and Glu. The experimental results demonstrate that the MIP/$CeO_2$ sensor exhibits exceptional capabilities in selectively identifying TAM even in the presence of these interferents.

This high selectivity can be attributed to the presence of imprinted cavities on the surface of the MIP/$CeO_2$ nanostructure, which are tailored to match the shape, size, and functional groups of TAM molecules. The interference factor for analytes in the presence of TAM was evaluated, confirming that the MIP/$CeO_2$ sensor functions effectively as a probe for the quantitative detection of TAM.

Figure 8b compares the response selectivity of both MIP/$CeO_2$ and NIP/$CeO_2$ nanostructures as sensing areas on an optical fiber based on LMR towards TAM and interfering drugs (DA, Glu, and Ep) at a concentration of 20 $\mu$M. The selectivity was quantified using the imprinting factor (IF), defined as $IF = \frac{R_{MIP}}{R_{NIP}}$, where $R_{MIP}$ and $R_{NIP}$ are the response ratios of the target sensor MIP to non-imprinted polymer. The obtained IF value for TAM was found to be 4.1, indicating a strong selective response compared to other interfering drugs. Typically, an IF above 2 is considered acceptable, while values above 4 or 5 indicate strong imprinting efficiency and high selectivity. The IF values above 4 are generally considered highly selective, reinforcing the effectiveness of our sensor, that indicating that the MIP has a significantly stronger affinity for the target molecule than the NIP.

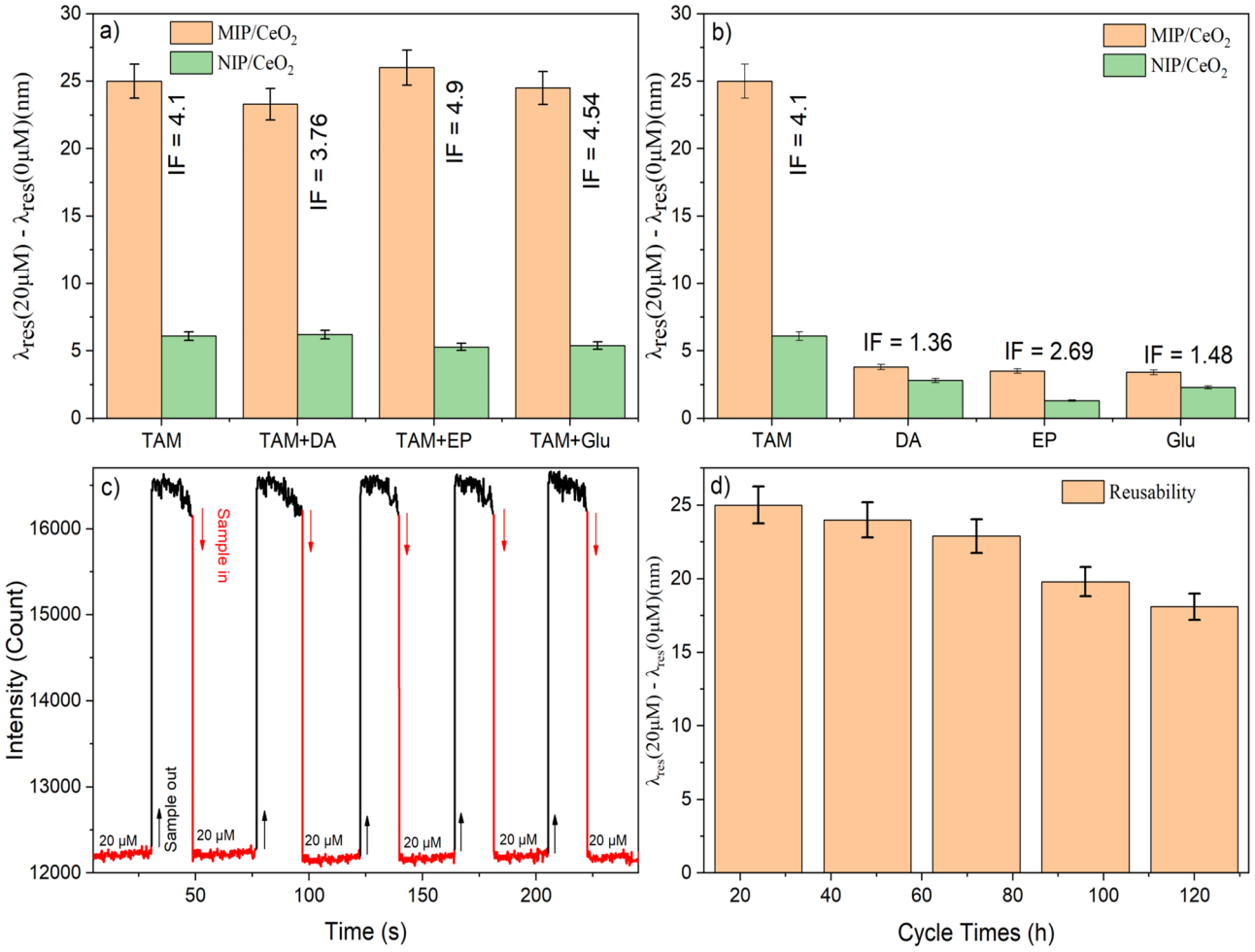


**Fig. 8**. Selectivity responses of the MIP/$CeO_2$ nanocomposite sensor. (**a**) Response to various interfering substances at a TAM concentration of 20 $\mu$M. (**b**) Selectivity towards different analytes, including TAM and potential interferents such as dopamine (DA), glucose (Glu), and epinephrine (Ep). (**c**) Assessment of the repeatability of the sensor's response over multiple trials. (**d**) Stability and reusability plot demonstrating the long-term performance of the sensor probe. The high imprinting factor (IF = 4.1) indicates strong selectivity for TAM, confirming the sensor's effectiveness in distinguishing TAM from other substances.

This high IF value demonstrates that the MIP/$CeO_2$ biosensor possesses excellent selectivity and sensitivity for quantitative detection of TAM.

To further assess the stability of the optical fiber sensor, the intensity spectrum was measured over a duration of 250 seconds. Measurements were conducted with a sample both without analyte and with a 20 $\mu$M analyte placed near the probe during each measurement cycle. This process was repeated six times, with results shown in Fig. 8c indicating consistent stability of the MIP/$CeO_2$ biosensor over time.

Additionally, Fig. 8d illustrates the long-term performance of the MIP/$CeO_2$ sensor within the specified timeframe. To validate its practicality, we measured output intensity with and without analyte presence. The repeatability of the sensor for detecting TAM was examined over five separate trials conducted within a 24-h period. The device demonstrated reliable performance over a testing duration of up to 120 h, showing only a minimal decrease in sensitivity (5 nm shift) compared to its initial response.

These findings highlight not only the high selectivity and sensitivity of the MIP/$CeO_2$ biosensor for TAM detection but also its robustness and reliability for practical applications in biomedical diagnostics.

*Detection and quantification limits*

In analytical chemistry, LOD values vary depending on the method, butvalues below 1 $\mu$M are often considered highly sensitive for biosensors. A higher LOQ ensures reliable quantification, reducing measurement uncertainty. LOQ values below 5 $\mu$M are generally considered ideal for biosensors detecting pharmaceutical compounds. For the MIP/$CeO_2$ nanostructured probes prepared on an optical fiber with a diameter of 550 $\mu$m, the calculated LOD was found to be 0.0942 $\mu$M, while the LOQ was determined to be 0.2853 $\mu$M. These values indicate that the sensor is capable of detecting very low concentrations of TAM, making it suitable for applications in clinical settings where precise drug measurement is essential.

The ability to detect TAM at such low concentrations is particularly advantageous in clinical medicine, where accurate quantification of drug levels in patients is crucial for therapeutic monitoring. The innovative use of polymer optical fiber technology combined with LMR provides a robust solution for TAM detection.

Table 2 presents a comprehensive overview of various technologies employed for TAM detection, highlighting the advantages of POF sensors over traditional methods. These advantages include improved linearity, enhanced stability, lower LODs, cost-effectiveness, increased surface sensitivity, and faster assay times.

The high selectivity and sensitivity of the MIP/$CeO_2$ biosensor for TAM not only demonstrate its potential for practical applications but also underscore its role in advancing analytical techniques in biomedical diagnostics. By utilizing these advanced sensing technologies, clinicians can achieve more reliable and efficient monitoring of therapeutic drug levels, ultimately leading to better patient outcomes.

*Real sample testing*

The effectiveness of the LMR-based optical fiber sensor for detecting tamoxifen was evaluated through its application to real samples, including pharmaceutical tablets and serum. The optical sensor's performance demonstrated a promising recovery rate for TAM, ranging from 102.20% to 96.01%, as detailed in Table 3. These recovery rates indicate that the MIP/$CeO_2$ nanostructure effectively maintains its ability to identify TAM in complex matrices.

The high recovery percentages suggest that the sensor can accurately quantify TAM even in the presence of other components typically found in pharmaceutical formulations. This capability is particularly significant in clinical settings where precise drug monitoring is essential for effective treatment regimens. A low Relative Standard Deviation (RSD) signifies excellent repeatability and minimal variation across multiple measurements. In biosensor applications, an RSD below 2% is generally regarded as highly stable, ensuring consistent performance. According to international biosensor validation guidelines, an RSD under 1% is ideal for analytical methods, confirming the robustness of the developed sensor.

| Technique | Transducer | Bio-recognition element | LOD | Detection range | Validation solution | Reference |
|---|---|---|---|---|---|---|
| Fluorimetry | Coumarin | MIP | - | - | - | 37 |
| Chemiluminescence | Mn(IV) with formaldehyde | MIP | 40 ng/mL | 100 ng/mL - 1 $\mu$g/mL | Pretreated human urine | 38 |
| Electrical impedance photolithography | Ti/Au film | Electrode | - | 12.5 - 37.5 $\mu$M | Cervical cancer cells | 10 |
| Electrochemical | N-CQD/$Fe_3O_4$ | Electrode | - | 0.04 - 320 $\mu$M | Phosphate buffer solution | 39 |
| Electrochemical | GO-CuO | Modified pencil graphite electrode | 39.65 $\mu$mol/L | 40 $\mu$mol/L | Pharmaceutical serum | 40 |
| Electrochemical | $Al_2O_3$@C/$V_2O_5$ | Modified electrode | 0.025 mM | 0.1 - 200 $\mu$M | Drug samples | 41 |
| Electrochemical | $SiO_2$ nanoparticles | Modified electrode | - | - | Buffer solution | 42 |
| Optical Fiber Sensor | Ag/$Yb_2O_3$ nanostructures | MIP | 0.0987 $\mu$M | 0.1 - 20 $\mu$M | Water/ Methanol mixture | 30 |
| Optical Fiber Sensor | $CeO_2$ nanoparticles | MIP/$CeO_2$ nanostructure | 0.0942 $\mu$M | 0.1 - 20 $\mu$M | Water/ Methanol mixture | This Work |

**Table 2**. Comparison of detection techniques for TAM with the findings of this study.

| Sample | Added ($\mu$M) | Expected ($\mu$M) | Found ($\mu$M) | Recovery (%) | RSD(%, n = 3) |
|---|---|---|---|---|---|
| Tablet* | 0.00 | 15.00 | 14.40 | 96.01 | 0.31 |
| | 5.00 | 20.00 | 19.29 | 96.43 | 0.35 |
| | 10.00 | 25.00 | 25.24 | 100.96 | 0.26 |
| Pharmaceutical serum** | 10.00 | 10.00 | 9.67 | 96.69 | 0.15 |
| | 15.00 | 15.00 | 14.63 | 97.53 | 0.19 |
| | 20.00 | 20.00 | 20.44 | 102.20 | 0.49 |

**Table 3**. Accuracy and recovery test results for tamoxifen detection in real samples. *Iran Hormone Pharmaceutical Company, Tehran, Iran (20 mg tablet). **Dextrose (3.33%), Saline (0.3%), Iranian Parenteral Pharmaceutical Co., Tehran, Iran

Furthermore, the results underscore the potential of the LMR-based sensor for practical applications in TAM detection, highlighting its robustness and reliability when applied to real-world samples. The integration of MIPs into the sensor design not only enhances selectivity but also improves sensitivity, making it a valuable tool for therapeutic drug monitoring.

## Conclusion

In summary, we successfully developed a LMR-based optical fiber sensor for the sensitive detection of TAM using a MIP combined with $CeO_2$ nanostructures. This innovative sensor was experimentally fabricated, demonstrating significant advancements in the field of drug detection. The optimization of the transmissivity of the thin layer and surrounding materials facilitated the generation of LMR, resulting in a notable shift of 25 nm in the resonance wavelength observed in the transmission spectrum. The sensitivity of the proposed sensor was quantified at 12.052 nm/$\mu$M, enabling the detection of TAM at concentrations as low as 0.1 $\mu$M. Furthermore, we established LOD and LOQ at 0.09416 $\mu$M and 0.28533 $\mu$M, respectively, with a high correlation coefficient ($R^2$) of 0.988 and an imprinting factor of 4.10. These metrics highlight the sensor's exceptional performance and reliability. The findings indicate that the MIP/$CeO_2$ biosensor is not only effective for rapid and accurate determination of TAM but also holds considerable promise for practical applications in clinical settings where precise drug monitoring is crucial. Future work may explore the integration of this sensor into point-of-care testing devices, enhancing its applicability in real-world scenarios.

## Data availability

All data generated or analysed during this study are included in this published article.

Received: 8 April 2025; Accepted: 20 June 2025
Published online: 29 July 2025

## References

1. Azargoshasb, T., Navid, H. A., Parvizi, R. & Heidari, H. Evanescent wave optical trapping and sensing on polymer optical fibers for ultra-trace detection of glucose. *ACS Omega* **5**, 22046–22056 (2020).
2. Figueira, R. B., de Almeida, J. M., Ferreira, B., Coelho, L. & Silva, C. J. Optical fiber sensors based on solgel materials: design, fabrication and application in concrete structures. *Mater. Adv.* **2**, 7237–7276 (2021).
3. Benítez, M., Zubiate, P., Del Villar, I., Socorro-Leránoz, A. B. & Matías, I. R. Lossy mode resonance based microfluidic platform developed on planar waveguide for biosensing applications. *Biosensors* **12**, 403 (2022).
4. Gaur, D. S., Purohit, A., Mishra, S. K. & Mishra, A. K. An interplay between lossy mode resonance and surface plasmon resonance and their sensing applications. *Biosensors* **12**, 721 (2022).
5. Kanberoglu, G. S., Coldur, F., Topcu, C. & Cubuk, O. Pvc-membrane potentiometric sensor for the determination of tamoxifen in pharmaceutical formulations. *IEEE Sens. J.* **15**, 6199–6207 (2015).
6. Gupta, B. D. & Semwal, V. Recent advances in molecular imprinting technique based fiber optic biosensors. *Opt. Fiber Technol.* **80**, 1456 (2023).
7. Betlem, Kai et al. Development of a flexible mip-based biosensor platform for the thermal detection of neurotransmitters. *MRS Adv.* **3**(28), 1569–1574 (2018).
8. Beiki, T., Najafpour-Darzi, G., Mohammadi, M., Shakeri, M. & Boukherroub, R. Fabrication of a novel electrochemical biosensor based on a molecular imprinted polymer-aptamer hybrid receptor for lysozyme determination. *Anal. Bioanal. Chem.* **415**, 899–911 (2023).
9. Yarman, A. & Scheller, F. W. The first electrochemical mip sensor for tamoxifen. *Sensors* **14**, 7647–7654 (2014).
10. Pradhan, R., Kalkal, A., Jindal, S., Packirisamy, G. & Manhas, S. Four electrode-based impedimetric biosensors for evaluating cytotoxicity of tamoxifen on cervical cancer cells. *RSC Adv.* **11**, 798–806 (2021).
11. Uygun, Z.O., Uygun, H.D.E., Ermiş, N., & Canbay, E. Molecularly imprinted sensors—new sensing technologies. In *Biosensors–Micro and Nanoscale Applications* 85–108 (2015).
12. Park, R. et al. Recent advances of point-of-care devices integrated with molecularly imprinted polymers-based biosensors: From biomolecule sensing design to intraoral fluid testing. *Biosensors* **12**, 136 (2022).
13. Di Giulio, T., Mazzotta, E. & Malitesta, C. Molecularly imprinted polyscopoletin for the electrochemical detection of the chronic disease marker lysozyme. *Biosensors* **11**, 3 (2020).
14. Herrera-Chacón, A., Cetó, X. & Del Valle, M. Molecularly imprinted polymers-towards electrochemical sensors and electronic tongues. *Anal. Bioanal. Chem.* **413**, 6117–6140 (2021).
15. Lin, Z.-T., DeMarr, V., Bao, J. & Wu, T. Molecularly imprinted polymer-based biosensors: for the early, rapid detection of pathogens, biomarkers, and toxins in clinical, environmental, or food samples. *IEEE Nanatechnol. Mag.* **12**, 6–13 (2018).
16. Singh, K. R., Nayak, V., Sarkar, T. & Singh, R. P. Cerium oxide nanoparticles: properties, biosynthesis and biomedical application. *RSC Adv.* **10**, 27194–27214 (2020).

17. Naidi, S. N., Khan, F., Tan, A. L., Harunsani, M. H., Kim, Y.-M., & Khan, M. M. Green synthesis of $ceo_2$ and zr/sn-dual doped $ceo_2$ nanoparticles with photoantioxidant and antibiofilm activities (2021).
18. Ahmad, A. et al. Green synthesized ag decorated $ceo_2$ nanoparticles: efficient photocatalysts and potential antibacterial agents. *Chemosphere* **310**, 136841 (2023).
19. Nadeem, M. et al. Green synthesis of cerium oxide nanoparticles ( $ceo_2$ nps) and their antimicrobial applications: a review. *Int. J. Nanomed.* **15**, 5951–5961 (2020).
20. Naidi, S. N., Harunsani, M. H., Tan, A. L. & Khan, M. M. Green-synthesized $ceo_2$ nanoparticles for photocatalytic, antimicrobial, antioxidant and cytotoxicity activities. *J. Mater. Chem. B* **9**, 5599–5620 (2021).
21. Guan, P., Li, Y., Zhang, J. & Li, W. Non-enzymatic glucose biosensor based on cuo-decorated $ceo_2$ nanoparticles. *Nanomaterials* **6**, 159 (2016).
22. Radhakrishnan, S., Kim, B.-S., & Dave, S. Surface modification with nanomaterials for electrochemical biosensing application. In *Advanced Nanomaterials for Point of Care Diagnosis and Therapy* 101–120 (Elsevier, 2022).
23. El Khalifi, M., Picaud, F. & Bizi, M. Electronic and optical properties of $ceo_2$ from first principles calculations. *Anal. Methods* **8**, 5045–5052 (2016).
24. Vangelista, S. et al. Structural, chemical and optical properties of cerium dioxide film prepared by atomic layer deposition on tin and si substrates. *Thin Solid Films* **636**, 78–84 (2017).
25. Shcherbakov, A. B. et al. $Ceo_2$ nanoparticle-containing polymers for biomedical applications: a review. *Polymers* **13**, 924 (2021).
26. Reviewed, Peer. Molecular imprinting: new possibilities for sensor technology. *Anal. Chem.* **69**(11), 345A-349A (1997).
27. Wang, Xu.-dong & Wolfbeis, Otto S. Fiber-optic chemical sensors and biosensors (2015–2019). *Anal. Chem.* **92**(1), 397–430 (2020) (**PMID: 31665884**).
28. Azargoshasb, T., Parvizi, R., Bozorgzadeh, F., Navid, H. A. & Heidari, H. Smart green cqd@ $sio_2$ hybrid coated optical fiber manifesting dual versatile absorptive and mip features towards epinephrine detection. *Nanoscale Adv.* **5**, 459–470 (2023).
29. Haupt, Karsten & Mosbach, Klaus. Molecularly imprinted polymers and their use in biomimetic sensors. *Chem. Rev.* **100**(7), 2495–2504 (2000).
30. Sadeghfar, F., Nikbakht, M. & Parvizi, R. Green synthesis of ag/ $yb_2$ $o_3$ nanostructures based-mip for tamoxifen detection: advancing from refractometers to sensor. *J. Mol. Struct.* **1309**, 138110 (2024).
31. Swanepoel, R. Determination of the thickness and optical constants of amorphous silicon. *J. Phys. E: Sci. Instrum.* **16**(12), 1214 (1983).
32. Yusof, N. A., Zakaria, N. D., Maamor, N. A. M., Abdullah, A. H. & Haron, M. J. Synthesis and characterization of molecularly imprinted polymer membrane for the removal of 2,4-dinitrophenol. *Int. J. Mol. Sci.* **14**, 3993–4004 (2013).
33. Umar, A. et al. Nitroaniline chemi-sensor based on bitter gourd shaped ytterbium oxide ( $yb_2$ $o_3$) doped zinc oxide (zno) nanostructures. *Ceram. Int.* **45**, 13825–13831 (2019).
34. Aziz, S. B. et al. Synthesis of pva/ $ceo_2$ based nanocomposites with tuned refractive index and reduced absorption edge: structural and optical studies. *Materials* **14**, 1570 (2021).
35. Lépinay, S., Ianoul, A. & Albert, J. Molecular imprinted polymer-coated optical fiber sensor for the identification of low molecular weight molecules. *Talanta* **128**, 401–407 (2014).
36. Taravideh, K., Parvizi, R. & Sadeghi, E. Efficient all-optical $mos_2$/au hybrid plasmon-exciton competitive response towards selective gas sensors. *Photon. Nanostruct. Fundam. Appl.* **54**, 101131 (2023).
37. Ray, J. V. et al. Smart coumarin-tagged imprinted polymers for the rapid detection of tamoxifen. *Anal. Bioanal. Chem.* **408**, 1855–1861 (2016).
38. Nie, F., Lu, J., He, Y. & Du, J. Use of molecule imprinting chemiluminescence method for the determination of tamoxifen in breast cancer sufferers' urine. *Lumin. J. Biol. Chem. Lumin.* **20**, 315–320 (2005).
39. Shalali, F., Cheraghi, S. & Taher, M. A. A sensitive electrochemical sensor amplified with ionic liquid and n-cqd/ $fe_3$ $o_4$ nanoparticles for detection of raloxifene in the presence of tamoxifen as two essential anticancer drugs. *Mater. Chem. Phys.* **278**, 125658 (2022).
40. Fouladgar, M., Karimi-Maleh, H., Opoku, F. & Govender, P. P. Electrochemical anticancer drug sensor for determination of raloxifene in the presence of tamoxifen using graphene-cuo-polypyrrole nanocomposite structure modified pencil graphite electrode: theoretical and experimental investigation. *J. Mol. Liq.* **311**, 113314 (2020).
41. Soltani, N. et al. Electrochemical measurement of tamoxifen in the presence of acetaminophen and ascorbic acid using carbon paste electrode modified with novel nanoparticles. *Microchem. J.* **183**, 108016 (2022).
42. Heydari, E., Raoof, J. B., Ojani, R. & Bagheryan, Z. $Sio_2$ nanoparticles modified cpe as a biosensor for determination of i-motif dna/tamoxifen interaction. *Int. J. Biol. Macromol.* **89**, 421–427 (2016).


## Author contributions

Fardin Sadeghfar: Writing – original draft, Software, Methodology, Investigation, Formal analysis, Data curation, Conceptualization. Roghaieh Parvizi: Project administration, Validation, Investigation, Formal analysis, Conceptualization. Moladad Nikbakht: Writing – review & editing, Validation, Supervision, Investigation, Formal analysis, Data curation, Conceptualization.


## Funding

The authors received no specific funding for this work.


## Competing interests

The authors declare no competing interests.

## Additional information

**Correspondence** and requests for materials should be addressed to M.N.